# 3D Visualisation of chemical shielding tensors (VIST) to elucidate aromaticity and antiaromaticity†

Felix Plasser[*a] and Florian Glöcklhofer[b]

Aromaticity is a central concept in chemistry, pervading areas from biochemistry to materials science. Recently, synthetic chemists started to exploit more intricate phenomena such as the interplay of local and global (anti)aromaticity as well as aromaticity in non-planar systems and three dimensions. These phenomena pose new challenges in terms of our fundamental understanding and the practical visualisation of aromaticity, its local variations and anisotropy. To overcome these challenges, a method for the visualisation of chemical shielding tensors (VIST) is developed here. The VIST method is based on nucleus-independent chemical shifts but, in contrast to other methods, allows for a 3D visualisation with quantitative information about the local variations and anisotropy of the chemical shielding. The VIST method is exemplified in benzene to show its main properties, in phenanthrene to highlight various degrees of local aromaticity, and in cyclobuta[l]phenanthrene to illustrate the interplay between local aromaticity and antiaromaticity in its singlet ground state and Baird aromaticity in its triplet excited state. Subsequently, the interplay of local and global aromaticity is investigated in two non-planar macrocycles, paracyclophanetetraene and [8]cycloparaphenylene, exemplifying the unique benefits of the VIST method for studying (anti)aromaticity in molecules with competing π-conjugated systems aligned in different planes. Finally, a stacked norcorrole dimer is studied, showing clear evidence of through-space aromaticity. In summary, we believe that the VIST method will be a highly valuable addition to the computational toolbox of chemists studying (anti)aromaticity or considering it in their molecular design.
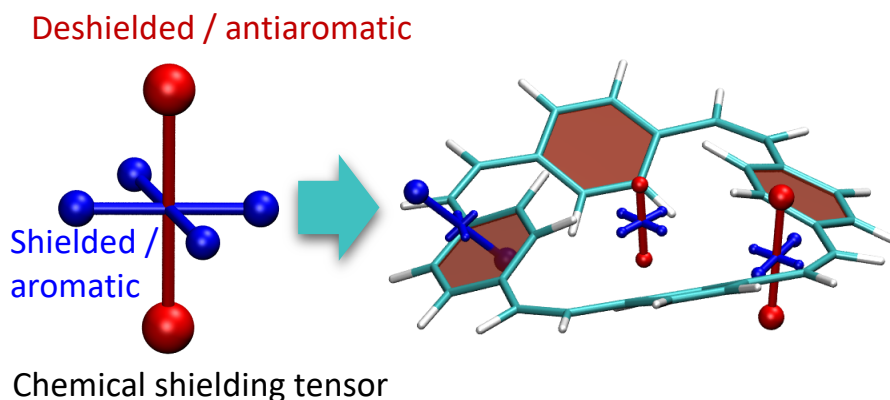
1 Introduction

The concept of aromaticity has intrigued chemists for over 200 years[1] and is a fundamental ingredient in our understanding of the properties and reactivity of molecules. Aromatic molecules play central roles in many areas of chemistry, such as organic chemistry, biochemistry, photochemistry, and molecular materials science. More recently, chemists also started to consider local aromatic effects and antiaromaticity in the design of organic materials offering promising applications based on fascinating chemistry. The field of singlet fission,[2] as one prominent example, has been invigorated by both ideas, and the modulation of local aromaticity via the insertion of heteroatoms[3,4] and the interplay of ground-state antiaromaticity with triplet excited-state aromaticity[5–7] have lead to a new push in the quest of designing molecules with the desired energies of their singlet and triplet excited states. Moreover, application of Clar's sextet theory[8] to control local aromaticity provides a powerful way of tuning biradical character and, thus, opening the route to a range of optoelectronic applications.[9–12]

A new and exciting frontier is opened in terms of macrocycles and larger π-conjugated systems, in which local and global (anti)aromaticity can both play a role. Here, (anti)aromaticity is being studied in systems as diverse as nanographenes,[13,14] porphyrin nanorings,[15,16] carbon nanobelts,[17] cyclocarbon,[18] cycloparaphenylenes,[19] cycloparaphenylmethine,[20] paracyclophanetetraene,[21] norcorrole[22,23] and other porphyrinoids.[24,25] Several of these systems are interesting due to their remarkable capacity to stabilise multiply charged ions[19] making them promising candidates for organic battery electrodes.[21,26,27] Excited-state (triplet) aromaticity[28,29] and Möbius aromaticity are also being investigated,[30–33] as well as three-dimensional aromaticity

in stacked systems,[34] cyclophanes,[35] π-conjugated cages,[36] and borane cages.[37] Finally, homoaromaticity provides yet another fascinating field of non-standard aromaticity[38–41] with potential applications in mechanoresponsive materials.[40]

Considering the ubiquity of aromaticity in chemistry and its diverse appearances, there has been a strong push toward the development of methods to visualise and quantify aromaticity in different instances. The most fundamental qualitative characterisation, still widely applied today, goes back to Erich Hückel[42,43] simply stating that a cyclic π-conjugated system is aromatic (antiaromatic) if it contains $4n + 2$ ($4n$) π-electrons. However, in many cases a more detailed picture is desired and a number of methods for analysing aromaticity have been developed, many of which are related to the characteristic signals of (anti)aromatic systems in nuclear magnetic resonance (NMR) spectroscopy. Popular methods rely on current densities, such as the anisotropy of the induced current density (ACID)[44] or the gauge including magnetically induced current (GIMIC).[45] These methods are good for visualising delocalised electrons and ring currents, but they do not provide a quantitative aromaticity criterion.

A prominent quantitative measure for aromaticity is provided by the nucleus-independent chemical shifts (NICS).[46] In its basic form, the NICS value is just one number, the negative of the isotropically averaged chemical shielding computed at the centre of the ring of interest. To obtain more detailed insight, also its individual components, e.g. NICS$_{zz}$, are often reported.[47,48] To visualise chemical shielding in the context of the molecular structure, it has been suggested to compute the NICS values on a grid around the molecule of interest.[49–52] In this spirit, several recent applications present 1D scans, 2D contour plots or even 3D isosurfaces of the isotropic NICS values, e.g. to visualise local aromatic and antiaromatic parts of larger molecules,[6,22,35,53] to represent Clar sextets in condensed hydrocarbons,[54] or to study interactions in excimers.[55] These visualisations are almost exclusively based on isotropic NICS values. However, new challenges come into play in macrocycles and multi-ring systems where several ring-currents in different planes interact, possibly resulting in strong magnetic anisotropy. To overcome this problem it would be greatly beneficial to have a method for the 3D visualisation of the full underlying shielding tensor.

The purpose of this work is to develop such a method, denoted VIST (visualisation of the chemical shielding tensors). VIST will allow us to visualise local variations in aromaticity and antiaromaticity in the context of the molecular structure while also providing insight into the anisotropy of the chemical shielding. Briefly spoken, the method proceeds by computing the chemical shielding tensor at a given point in space, computing its principal axes via a diagonalisation, and showing them as a local coordinate system. The method is sketched in Fig. 1. In this example, there is one strong deshielded (antiaromatic) component shown in red and two weaker shielded (aromatic) components shown in blue. Any one of these tensor components relates to the ring currents in a plane perpendicular to it.

Within this work, we first discuss the underlying theory and working equations of the VIST method. Subsequently, we apply the method to benzene, phenanthrene, and cy-
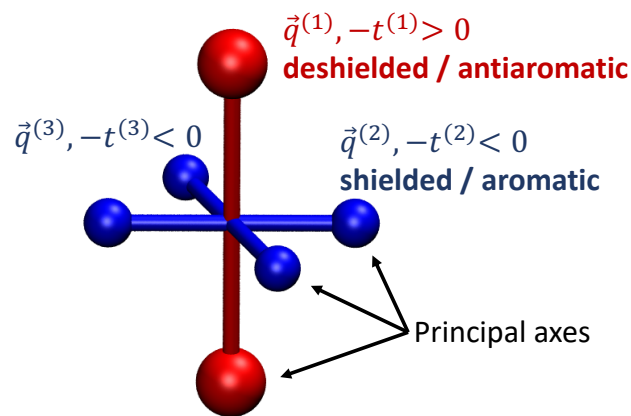

Fig. 1 3D visualisation of the chemical shielding tensor (VIST) via its three principal axes $\vec{q}^{(1)}$, $\vec{q}^{(2)}$, $\vec{q}^{(3)}$ and the associated eigenvalues $t^{(1)}$, $t^{(2)}$, $t^{(3)}$.

clobuta[l]phenanthrene to highlight the interplay of local aromaticity and antiaromaticity in these molecules. The full power of the VIST method is illustrated in three non-planar macrocyclic systems – paracyclophanetetraene (PCT), [8]cycloparaphenylene ([8]CPP), and a norcorrole dimer – to study the interplay of local aromaticity and antiaromaticity in these molecules and their variations for electronic states of different charge.

2 Methods

2.1 Definition of the chemical shielding tensors

The chemical shielding, which underlies nuclear magnetic resonance (NMR) spectroscopy, is generally defined as the mixed second derivative of the energy with respect to an external magnetic field B_β and the nuclear magnetic moment μ_γ[51,56,57]

$$\sigma_{\gamma\beta} = \frac{\partial^2 E}{\partial B_\beta \partial \mu_\gamma} \tag{1}$$

where β and γ are two Cartesian coordinates (x, y, z). Usually, the shielding is given as a sum of a diamagnetic $\sigma_{\gamma\beta}^{\mathrm{dia}}$ and paramagnetic $\sigma_{\gamma\beta}^{\mathrm{para}}$ term:

$$\sigma_{\gamma\beta} = \sigma_{\gamma\beta}^{\mathrm{dia}} + \sigma_{\gamma\beta}^{\mathrm{para}} \tag{2}$$

The properties of these terms have been discussed in great detail[51,57,58] and we shall only mention them briefly here. Assuming that the gauge origin lies at the point probed, we can write the diagonal z-component of the diamagnetic term as

$$\sigma_{zz}^{\mathrm{dia}} = \frac{\alpha^2}{2} \int \frac{x^2 + y^2}{r^3} \rho(\vec{r}) \mathrm{d}\vec{r} = \frac{\alpha^2}{2} \int \frac{\sin^2 \theta}{r} \rho(\vec{r}) \mathrm{d}\vec{r} \geq 0 \tag{3}$$

where α is the fine structure constant, $\rho(\vec{r})$ is the electron density at position $\vec{r}$, and θ is the angle from the z-axis. Analogous equations hold for $\sigma_{xx}^{\mathrm{dia}}$ and $\sigma_{yy}^{\mathrm{dia}}$. This term, related to the Lamb formula, represents the textbook view of NMR spectroscopy – the chemical shielding increases with the electron density $\rho(\vec{r})$ around the nucleus of interest.[58,59] Closer inspection of Eq. (3) shows that the chemical shielding in any given direction is determined by the electron distribution in the plane perpendicular to

it. Thus, ring currents in any given plane are represented by a pronounced tensor component perpendicular to that plane.

The paramagnetic term is usually given in a perturbative expansion[51,60] and, viewing again only its diagonal z-component at the gauge origin, we can write

$$\sigma_{zz}^{\text{para}} = -\alpha^2 \sum_{I \neq 0} \frac{\langle \Psi_0 | \hat{L}_z / r^3 | \Psi_I \rangle \langle \Psi_I | \hat{L}_z | \Psi_0 \rangle}{E_I - E_0} \tag{4}$$

where $\hat{L}_z$ denotes the angular momentum operator, Ψ_0 and Ψ_I are the ground and excited state wavefunctions, and E_0 and E_I are their energies. $\sigma_{zz}^{\text{para}}$ is generally a negative/deshielding term opposing the diamagnetic term.[58]

It is the idea behind the nucleus independent chemical shift (NICS) method[46] to compute the shielding not only at the nuclei, as relevant to NMR spectroscopy, but also at other points in space to gain insight into (anti)aromaticity. The NICS at any given point in space is defined as the negative of the isotropically averaged chemical shielding, i.e.

$$\text{NICS} = -\sigma_{\text{iso}} = -\frac{1}{3}(\sigma_{xx} + \sigma_{yy} + \sigma_{zz}). \tag{5}$$

Note that the chemical shielding and NICS are thus equivalent except for the sign and we shall use both terms interchangeably.

It is known that NICS values computed at the centre of an aromatic ring are negative, whereas they are positive for an antiaromatic ring.[46] Considering Eqs (3) and (4), we can rephrase this in the sense that for an aromatic system diamagnetic shielding dominates, whereas for an antiaromatic system paramagnetic deshielding dominates.[*] The diamagnatic shielding only depends on the distribution of the electrons in space and is, thus, present for aromatic and antiaromatic systems alike. Paramagnetic deshielding, on the other hand, has a more involved expression relying on the existence of low-energy excited states accessible through rotational transitions (cf. Refs 61,62) and becomes large in magnitude only for antiaromatic systems.

2.2 Visualisation of shielding tensors (VIST)

Following Eq. (1), it is seen that the chemical shielding is given as a non-symmetric 3×3 tensor containing 9 independent values. Whereas scalar-valued functions can be represented in 3D space *via* isosurfaces and vector-valued functions *via* arrows, it is necessary to construct a more involved representation for a tensor-valued function. Here, we suggest to do so by constructing the principal axes of the chemical shielding tensor as its eigenvectors in analogy to the principal axes of the moment of inertia. The eigenvectors $\vec{q}^{(1)}, \vec{q}^{(2)}, \vec{q}^{(3)}$ and eigenvalues $t^{(1)}, t^{(2)}, t^{(3)}$ are given as

$$\sum_{\beta \in \{x,y,z\}} \sigma_{\gamma\beta} q_\beta^{(i)} = t^{(i)} q_\gamma^{(i)} \qquad i \in \{1,2,3\} \tag{6}$$

---

[*] Note that the total shielding is invariant to the gauge origin but that the division between diamagnetic and paramagnetic contributions depends on the gauge origin chosen. The presented discussion, therefore, represents only one possible interpretation of the underlying physics.

For visualisation, we construct a local coordinate system oriented according to the eigenvectors $\vec{q}^{(i)}$ and visualise the three components as dumb-bells whose size and length depend on the absolute value of the associated eigenvalue $|t^{(i)}|$ and whose color depends on the sign (blue or red), see Fig. 1. Specifically, we draw the length L of the axis and the radius R of the sphere as

$$L = 2 \times 0.3\sqrt{|t^{(i)}|} \qquad R = 0.03\sqrt{|t^{(i)}|} \tag{7}$$

where $t^{(i)}$ is given in ppm and L and R are given in Å. Through encoding the eigenvectors and eigenvalues in the representation, we are able to represent the full information given in the 3×3 tensor graphically.

To compare these results to the NICS values, it is worth noting that in analogy to Eq. (5) the NICS value is a third of the sum of the three eigenvalues according to

$$\text{NICS} = -\sigma_{\text{iso}} = -\frac{1}{3}(t^{(1)} + t^{(2)} + t^{(3)}) \tag{8}$$

Finally, we want to point out that the shielding tensor is in general represented by a non-symmetric matrix, which gives rise to two technical points to consider: (i) the fact that the left and right eigenvectors are not the same and (ii) the occurrence of complex eigenvalues. Both points are discussed in Sec S1.[†]

2.3 Computational Details

Chemical shielding tensors were computed in Gaussian 09[63] using the PBE0 functional[64,65] along with the def2-SVP basis set[66] using gauge-including atomic orbitals[56] and applying tight SCF convergence criteria. Calculations on the singlet (triplet) states were performed using restricted (unrestricted) density functional theory. Molecular geometries of benzene, phenanthrene, cyclobuta[l]phenanthrene, PCT, and [8]CPP were optimised at the PBE0/def2-SVP level. Unless specified, shielding tensors were computed for geometries optimised for the respective spin/charge state. In the case of the stacked norcorrole dimer, the molecular geometry was taken from the crystal structure[35] with removed bithiophene linkers. The same structure, but with one monomer removed, was used for the monomer calculation.

We have implemented the VIST method within the TheoDORE wavefunction analysis package.[67-69] A first version of the code is scheduled to be released within TheoDORE 2.4. The visual molecular dynamics (VMD)[70] program is used as a graphical backend for creating the tensor representations in connection with molecular structures and isosurfaces. The signed current density modulus[71] of phenanthrene was computed using the GIMIC program.[45] ACID plots for PCT used the ACID program.[44]

The underlying research data (molecular geometries, Gaussian input/output files, and input scripts for VMD) are provided via a separate repository.[72]

3 Results and Discussion

Within this section, the VIST method is exemplified in a hierarchy of systems of increasing complexity. We start by discussing the basic elements of VIST in benzene, proceed by a discussion of local

variations in aromaticity in phenanthrene and continue by discussing the interplay of ground state antiaromaticity and triplet state Baird aromaticity in cyclobuta[l]phenanthrene. A detailed discussion of the anisotropy of the chemical shielding and its variation with the molecular charge is provided in two macrocyclic systems (PCT, [8]CPP). Finally, we illuminate the emergence of 3D through-space aromaticity in the case of two stacked norcorrole molecules.

(a) NICS(0) = -8.92
(-13.3/-6.74/-6.74)

(d) NICS(0) = -42.47
(-70.8/-43.8/-12.9)

(b) NICS(1) = -11.23
(-29.5/-2.10/-2.09)

(e) NICS(1) = -16.02
(-34.0/-7.02/-7.02)

(c) NICS(2) = -5.17
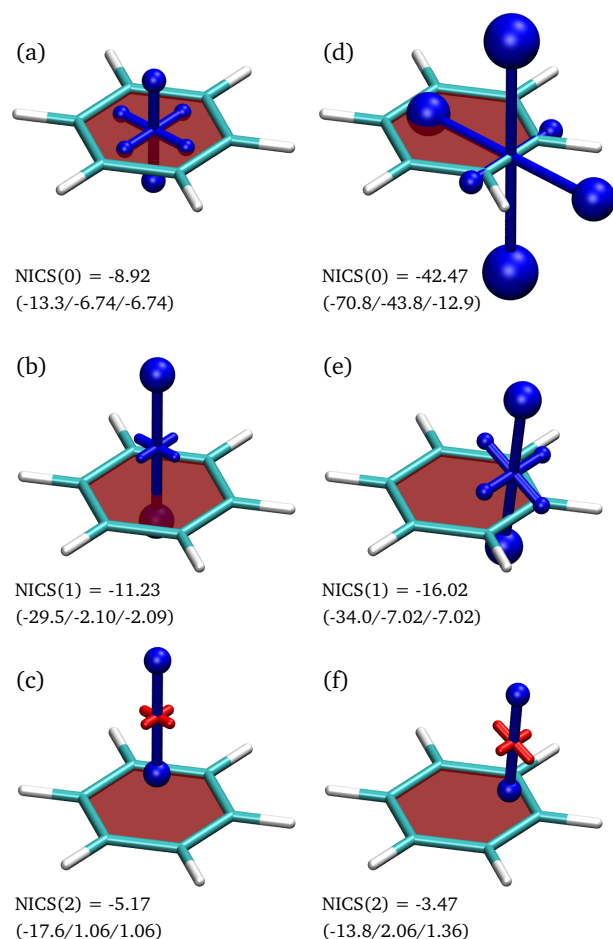(-17.6/1.06/1.06)

(f) NICS(2) = -3.47
(-13.8/2.06/1.36)

Fig. 2 3D visualisation of the chemical shielding tensors (VIST) in benzene. Negative (shielded/aromatic) contributions are shown in blue, positive (deshielded/antiaromatic) in red. Below the pictures, isotropic NICS values are given in ppm, the negatives of the associated eigenvalues $t^{(i)}$ are shown in parentheses. Shielding tensors were computed at (a) the centre of the molecule, (b) 1 Å and (c) 2 Å above the plane; (d) at the centre of a bond, (e) 1 Å and (f) 2 Å above the bond.

3.1 Benzene

Shielding tensors for benzene were computed at various positions around the molecule to examine how the shielding varies with the position, illustrating the basics of the VIST method (Fig. 2). The chemical shielding at the centre of the ring, also denoted NICS(0) is presented in Fig. 2 (a). The tensor representation shows a dominant out-of-plane component (-13.3 ppm) along with two smaller in-plane components (-6.7 ppm), which average to an overall isotropic NICS(0) value of -8.9 ppm. Due to the

high symmetry present, the out-of-plane eigenvalue is equivalent to the NICS(0)$_{zz}$ value, which has been reported as -13.2 ppm elsewhere,[47] in agreement with the present results. Fig. 2 (a) clearly shows that appreciable shielding is present along all three coordinate axes, which, in line with Eq. (3), can be understood in the sense that the centre of the ring is surrounded by electron density on all sides (see also Fig. S2†). To eliminate the influence of the bulk electron density and focus on in-plane currents in the π-system, the NICS value is often computed 1 or 2 Å above the molecular plane, denoted NICS(1) and NICS(2). The associated tensors are shown in panels (b) and (c), respectively, highlighting that the out-of-plane shielding deriving from in-plane ring currents increases in size whereas the in-plane shielding almost vanishes (see also Ref. [73]). The dominant contribution to NICS(1) is the out-of-plane component of -29.5 ppm, which has been ascribed to the π-electrons[47] and, thus, provides an expedient measure for aromaticity. The NICS(2) tensor is, again, dominated by the out-of-plane component and, interestingly, the in-plane components are slightly deshielded (red). Comparison to the electron density isosurface (Fig. S2) shows that the NICS(1) and NICS(2) values are computed well above the main part of the density and it is, thus, understandable that the chemical shielding tensor only "sees" the ring-currents in the aromatic ring rather than the bulk of the σ-electrons.

For comparison, also the shielding tensors along and above one of the CC bonds were computed [Fig. 2 (d-f)]. It is noteworthy that all NICS(0) eigenvalues are strongly enhanced when computed within the bond. The enhanced contributions can be understood in the sense that a higher electron density yields enhanced diamagnetic shielding according to Eq. (3), but this is obviously not related to aromatic ring currents. An enhancement of NICS values close to the bonds is also visible for NICS(1), in agreement with recent results of 2D and 3D scans.[22,54] This enhancement is lost in the case of the NICS(2) tensor in Fig. 2.

In summary, the above discussion highlights the importance of local variations in the overall chemical shielding and its individual tensor components. The VIST method proved to be an expedient method to visualise both phenomena.

3.2 Phenanthrene – variations in local aromaticity

Next we consider the phenanthrene molecule as an example of a polycyclic aromatic hydrocarbon with the goal of studying variations in its local aromaticity. The molecular structure of phenanthrene is shown in Fig. 3 (a). Here, we highlight the two Clar sextets on the outer rings, noting that putting the sextets on the sides is the only possibility of creating a resonance structure with two disjoint sextets and one, thus, expects the outer rings to have enhanced local aromaticity.[74] Indeed, when considering the NICS(0) values in Fig. 3 (b), we find that the outer rings (*A*) experience significantly enhanced shielding when compared to the inner ring (*B*). Interestingly, the out-of-plane component of NICS(0) computed at the centre ring almost vanishes. A comparison to benzene shows that the isotropic NICS(0) value at the outer rings is slightly higher for phenanthrene than benzene (-9.2 *vs* -8.9 ppm) but that the out-of-plane component is clearly

lower (-11.7 ppm *vs* -13.3 ppm). Before proceeding, it is worth noting that the NICS(0) values are not only strongly affected by the σ-system but that they are also expected to see strong effects from the magnetic fields induced by the neighbouring rings. For both reasons it is advantageous to proceed to the NICS(1) tensors shown in Fig. 3 (c). These have strong out-of-plane components in all three rings, representing strong in-plane aromaticity and, again, the outer rings are notably enhanced. The isotropic NICS(1) values as well as the individual tensor components of the side rings are very similar to benzene [Fig. 2 (c)] with the exception that the eigenvectors corresponding to the smaller contributions are slightly tilted out of plane.

(a)

(b)

A: NICS(0) = -9.16 (-11.68/-8.24/-7.56)
B: NICS(0) = -5.89 (-0.59/-8.32/-8.74)

(c)

A: NICS(1) = -11.49 (-29.47/-2.70/-2.31)
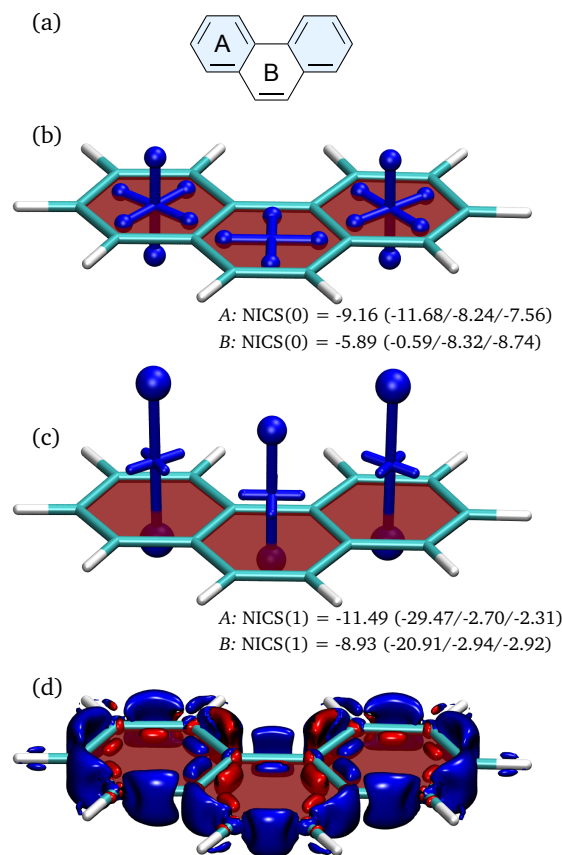*B:* NICS(1) = -8.93 (-20.91/-2.94/-2.92)

(d)

Fig. 3 Analysis of local aromaticity in phenanthrene: (a) molecular structure with Clar sextets highlighted in blue; 3D visualisation of the chemical shielding tensors (VIST, see Fig. 2 for details) computed at (b) the centre of each ring and (c) 1Å above the plane. NICS values (in ppm) are reported for the outer (*A*) and inner (*B*) rings. The isosurface of the current density modulus induced by a magnetic field in z-direction is shown in (d) (cutoff 0.1 a.u., blue - diatropic, red - paratropic).

For comparison, we also want to show a different representation of aromaticity,[71] which proceeds by computing the current density induced by a magnetic field perpendicular to the molecular plane and dividing the current into diatropic and paratropic contributions, which can roughly be understood as the currents giving rise to diamagnetic shielding [Eq. (3)] and paratropic deshielding [Eq. (4)], respectively. Diatropic and paratropic ring currents are shown in Fig. 3 (d) in blue and red. In line with pre-

vious results,[45,71] one finds diatropic ring currents outside of the bonds, extending over σ- and π-orbitals, and paratropic currents inside, deriving mainly from σ-orbitals. The diatropic currents (blue) dominate, explaining the net shielding seen in Fig. 3 (b) and (c). Closer inspection shows that the main paratropic contributions are located within the inner ring, explaining why shielding is reduced there, in particular for the NICS(0) tensors. The effect of these σ-contributions is reduced once one moves out of the molecular plane, explaining why strong shielding is obtained for all NICS(1) tensors.

In summary, we found that for a simple system like phenanthrene the isotropic NICS values already reflect the correct trends in terms of its variations in local aromaticity. However, the VIST method provides a detailed and intuitive representation of the individual shielding components, including the somewhat surprising result that the out-of-plane component at the inner ring almost vanishes. We have also highlighted that the visualisation of the current density can provide complementary information to the shielding tensors, thus, providing a combined strategy for illuminating intricate details of aromatic ring currents.

3.3 Cyclobuta[l]phenanthrene – antiaromaticity and Baird aromaticity

Whereas the previous two molecules were aromatic, we want to proceed by illustrating how the VIST method can be used particularly effectively to study the interplay of local aromaticity and antiaromaticity and their modulation via the electronic spin state. For this purpose, we add a cyclobutadiene (CBD) ring to phenanthrene to produce the cyclobuta[l]phenanthrene molecule. This molecule was reported as a potential singlet fission chromophore, owing to its low-energy first triplet state (<1eV) despite maintaining a large excitation energy of its first singlet excited state (>2eV).[6] The low triplet energy was explained by the combination of ground-state antiaromaticity and triplet-state Baird aromaticity of the CBD ring and we shall illustrate these phenomena below.

The molecular structure of cyclobuta[l]phenanthrene is shown in Fig. 4 (a), highlighting its aromatic Clar sextets in blue along with its antiaromatic CBD ring in red. The NICS(0) tensors of the singlet ground state presented in Fig. 4 (b) have a striking appearance with a strongly dominant out-of-plane antiaromatic (red) component on the CBD ring. The associated eigenvalue of 131.8 ppm is far higher in magnitude than any shielding value found in the above examples. Moving to the NICS(1) tensors in Fig. 4 (c) we find that antiaromaticity is still clearly visible but that the magnitude of the deshielding is strongly reduced (from 132 to 73 ppm for the dominant eigenvalue), a result also obtained for an isolated CBD molecule.[73,75] When viewing the phenanthrene part of the molecule, we find that the shielding tensors are only slightly perturbed as compared to isolated phenanthrene (Fig. 3).

Following Baird's rule,[28] one expects the four-membered CBD ring to exhibit aromaticity in its lowest triplet state. To examine this hypothesis, we have performed computations on this state. We start the discussion with the difference density between sin-
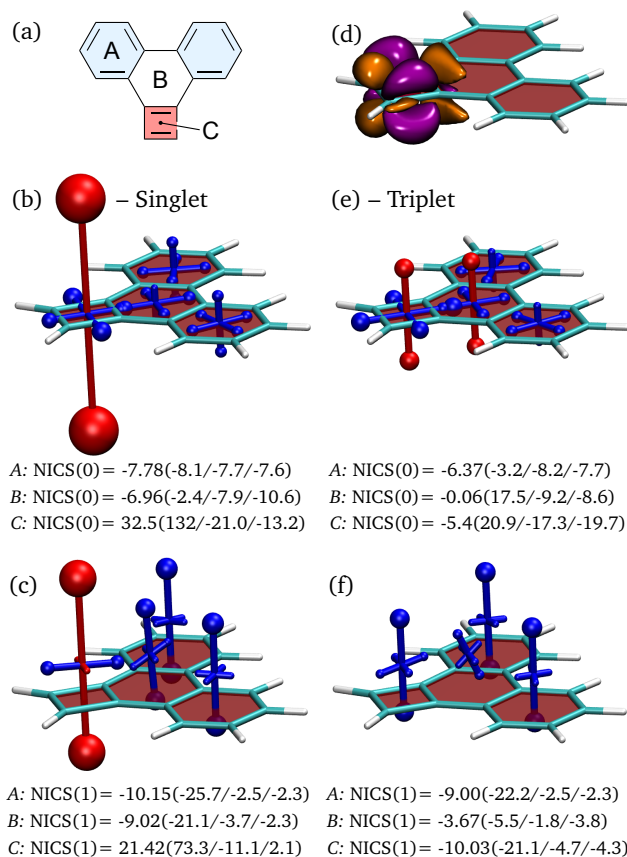
(a) [structure with rings A, B, C]

(d) [orbital image]

(b) – Singlet

(e) – Triplet

A: NICS(0) = -7.78(-8.1/-7.7/-7.6)
B: NICS(0) = -6.96(-2.4/-7.9/-10.6)
C: NICS(0) = 32.5(132/-21.0/-13.2)

A: NICS(0) = -6.37(-3.2/-8.2/-7.7)
B: NICS(0) = -0.06(17.5/-9.2/-8.6)
C: NICS(0) = -5.4(20.9/-17.3/-19.7)

(c)

(f)

A: NICS(1) = -10.15(-25.7/-2.5/-2.3)
B: NICS(1) = -9.02(-21.1/-3.7/-2.3)
C: NICS(1) = 21.42(73.3/-11.1/2.1)

A: NICS(1) = -9.00(-22.2/-2.5/-2.3)
B: NICS(1) = -3.67(-5.5/-1.8/-3.8)
C: NICS(1) = -10.03(-21.1/-4.7/-4.3)

Fig. 4 Analysis of local (anti)aromaticity in the lowest singlet and triplet states of cyclobuta[l]phenanthrene: (a) molecular structure with Clar sextets highlighted in blue and the antiaromatic ring in red; 3D visualisation of the chemical shielding tensors (VIST, see Fig. 2 for details) computed at (b)/(e) the centre of each ring and (c)/(f) 1 Å above the plane for the singlet/triplet; (d) difference density between singlet and triplet. NICS values (in ppm) are reported for the A, B, C positions as shown in (a).

glet and triplet to describe the electronic rearrangement involved. Fig. 4 (d) shows that the difference density is located on the CBD ring and, specifically, that the transition from the singlet to the triplet means a reduction (orange) in density along the bonds that are indicated as double bonds in Fig. 4 (a) and an enhancement (purple) in density on the other two bonds, resulting in an overall more even charge distribution around the CBD ring.

The change from singlet to triplet has a profound impact on the magnetic shielding, as shown in Fig. 4 (e, f), most importantly by eliminating the strongly deshielded component perpendicular to the CBD ring (C). Viewing the NICS(0) tensors [Fig. 4 (e)], we find that the CBD ring remains slightly deshielded while also the central 6-membered ring (B) obtains a slightly deshielded contribution. The z-components of the shielding tensors on the outer rings (A) are also reduced in magnitude, yielding a NICS$_{zz}$(0) value of only -3.2 ppm. Interpreting the NICS(0) contributions is not straightforward as it is not clear how to separate between the contributions from the π-electrons in the individual rings as well as the σ-electrons. Therefore, we also present the NICS(1) contributions to get a different viewpoint [Fig. 4 (f)]. Interestingly, the NICS(1) tensors all show pronounced aromaticity for the CBD

ring as well as the outer phenanthrene rings. It is noteworthy here that the values for the outer rings in phenanthrene (A) are almost unaltered between the singlet and triplet states, i.e. when comparing panels (c) and (f), suggesting that their π-electrons are not strongly perturbed by the excitation. The central ring (B), on the other hand, experiences a significant decrease in aromaticity. In summary, Fig. 4 (f) suggests to view the electronic structure of cyclobuta[l]phenanthrene in its triplet state as a combination of a Baird aromatic quartet with two Clar sextets (cf. Ref. [76]).

Finally, we note that strongly antiaromatic systems with emerging biradical character and low triplet energies would require a multireference treatment[77,78] for a reliable description of the wavefunctions involved, noting that NICS values and current densities may indeed be strongly affected by multireference effects.[75,79] Nonetheless, we believe that Fig. 4 provides a good, semiquantitative description of the relevant physics.

3.4 Paracyclophanetetraene – interplay of local aromaticity and global antiaromaticity in a macrocycle

Paracyclophanetetraene (PCT) is a non-planar macrocycle with competing π-conjugated systems aligned in different planes and, hence, a particularly challenging case for the purposes of visualising and quantifying its local variations in (anti)aromaticity. The macrocycle, as shown in Fig. 5 (a), features a π-conjugated perimeter of 24 [4n] π-electrons as well as four slightly twisted phenylene subunits with 6 [4n+2] π-electrons, each. In the neutral state, the macrocycle is formally antiaromatic but, in practice, was reported to not exhibit any measurable antiaromatic properties.[21] Twofold reduction, on the other hand, was reported to create a globally aromatic macrocyclic system of [4n+2] π-electrons whose enhanced stability renders PCT a promising new material for sodium-ion battery anodes.

Chemical shielding tensors were computed at three positions within the macrocycle: 1 Å off the plane of one of the phenylene rings (A), at the centre of the macrocycle (B), and on the side next to the double bond (C). Starting with the centre position (B), we find a deshielded component of 11.0 ppm along with two shielded components (-4.8 ppm) averaging to an isotropic NICS value close to zero. Moving closer to the side of the macrocycle (C) we find somewhat stronger deshielding (25.9 ppm), supporting the presence of global antiaromaticity for the macrocycle. However, it should be pointed out that part of the deshielding derives from diatropic currents in the benzene rings as shown in Fig. S3†, thus, indicating only weak antiaromatic character in line with the experimental observations.

Next, it is of interest to test the hypothesis of local aromaticity on the phenylene rings. For this reason, we have computed the NICS(1) tensor for one of the phenylene rings shown on the left in Fig. 5 (b). The tensor is tilted to be perpendicular to the phenylene ring but otherwise possesses a similar shape to the NICS(1) tensor of an isolated benzene molecule [Fig. 2 (b)] with only slightly reduced aromaticity (-24.2 vs -29.5 ppm for the dominant eigenvalue), thus, highlighting that the local aromaticity in the phenylene rings is largely unperturbed by the macrocycle. Note that the tilt seen in Fig. 5 (b) represents a non-trivial com-

(a)

(b) – Neutral

(d)

A: NICS(1) = -9.75 (-24.17/-3.28/-1.80)
B: NICS(0) = 0.44 (10.98/-4.83/-4.83)
C: NICS(0) = 4.38 (25.94/-4.48/-8.33)

(c) – Dianion

(e)

A: NICS(1) = -7.23 (-19.18/-2.55/0.05)
B: NICS(0) = -15.11 (-38.65/-3.35/-3.35)
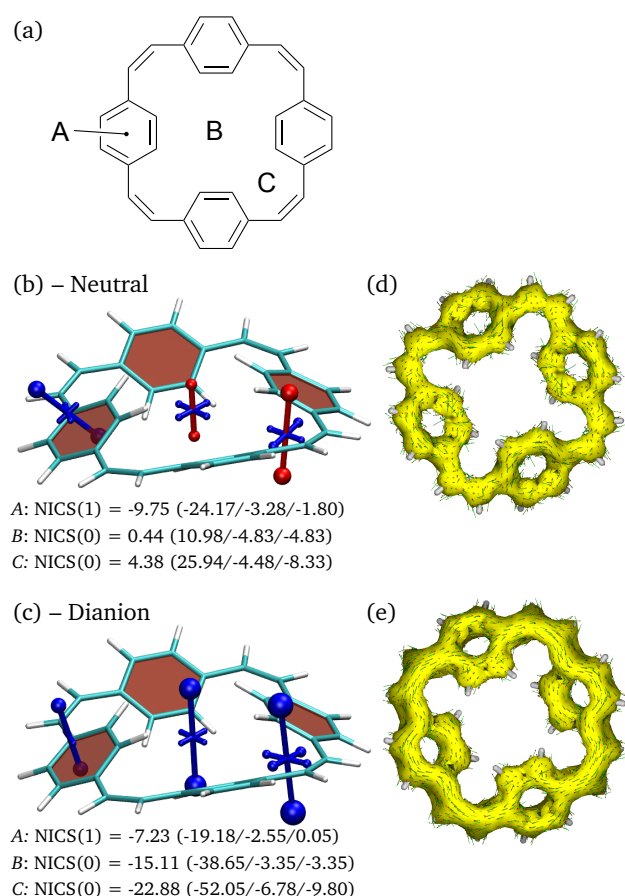C: NICS(0) = -22.88 (-52.05/-6.78/-9.80)

Fig. 5 Analysis of local (anti)aromaticity in paracyclophanetetraene: (a) molecular structure; 3D visualisation of the chemical shielding tensors (VIST, see Fig. 2 for details) for (b) the neutral and (c) the dianion – NICS values (in ppm) are reported for the phenylene ring (A), the centre (B), and side (C) of the macrocycle; ACID plots for (d) the neutral and (e) the doubly reduced form (isovalue 0.05).

bination of all the tensor components and would be difficult to comprehend without the VIST method.

The dianion shown in Fig. 5 (c) has a dramatically different appearance compared to the neutral state. Strong aromaticity (blue) perpendicular to the plane of the macrocycle is found for all three positions probed. The dominant eigenvalues obtained for positions B and C, -38.7 and -52.1 ppm, are even higher than the NICS(1)$_{zz}$ eigenvalue for benzene, shown in Fig. 2 (b). Viewing the phenylene position (A) one finds somewhat reduced shielding values and a tilt of the main component with respect to Fig. 5 (b) making it almost perpendicular to the plane of the macrocycle. These findings indicate that the local aromaticity of the phenylene ring is perturbed to allow for enhanced global aromaticity.

For comparison we also want to show the ACID plots[44] of the neutral and doubly reduced form, Fig. 5 (d,e). The isosurfaces shown represent the delocalised electrons whereas the small arrows represent the direction of the current if a magnetic field is applied in z-direction. The ACID plots are well-suited for highlighting that electron delocalisation extends over all carbon atoms in the macrocycle in both states shown. They show that there is

more delocalisation in the dianion than in the neutral state, supporting its global aromaticity. The dianion [Fig. 5 (e)] also shows arrows clearly going in clockwise direction, representing the large diatropic ring current that is responsible for the strong shielding seen in Fig. 5 (c). Conversely, it is not possible to identify the paratropic ring currents in panel (d) that are responsible for the deshielding found in the netural state. It is even challenging to locate the local diatropic ring currents in the phenylene units that give rise to their local aromaticity, which is unambiguously seen in Fig. 5 (b).

In summary, Fig. 5 underscores the dramatic changes PCT undergoes upon twofold reduction, explaining its remarkable redox properties. The ACID plots were useful for highlighting the overall electron distribution but the new VIST method provided a more direct representation of the remarkable changes in electronic structure, directly showing the switch from local to global aromaticity as brought forward by Eder et al.[21]

3.5 Cycloparaphenylene

Cycloparaphenylenes (CPP), macrocycles composed of phenylene units connected in *para*-position, are an intensively investigated class of conjugated macrocycles.[19,80] CPPs are attracting interest due to their unique optoelectronic properties[81,82] in combination with their rich host-guest chemistry[83] providing a promising basis for applications from solid-state nanomaterials to biological imaging.[84] When viewing the global properties of CPP macrocycles, every phenylene unit contributes 4 π-electrons to the macrocyclic π-conjugated pathway, meaning that any [n]CPP (where n represents the number of phenylene units) has 4n electrons in its π-conjugated pathway and is, thus, expected to be antiaromatic. Two-fold oxidation or reduction creates global aromaticity,[19] in line with the discussion on PCT in the last section.

An analysis of the neutral molecule is presented in Fig. 6 (a). Chemical shielding tensors were computed along a line going from the centre of one phenylene ring to the centre of a phenylene ring on the opposite side. Inside the macrocycle, one finds a slight deshielding (red) of up to 3.7 ppm in the out-of-plane direction. However, this is compensated by in-plane shielding and the isotropic NICS values inside the ring are all negative, in agreement with Ref. 19. When chemical shielding tensors are computed close to a phenylene ring, as shown on the left, one finds that they are strongly tilted as these now represent local aromaticity in the phenylene rings, which lie perpendicular to the plane of the macrocycle.

Next, we present computations on the dication, which was reported to exhibit strong global aromaticity.[19] Indeed, viewing Fig. 6 (b), we find strong shielded (blue) tensor components perpendicular to the plane of the macrocycle. At the centre of the ring, we find an out-of-plane NICS component of -36.4 ppm, which is similar to the dianion of PCT as shown in Fig. 5 (c), and slightly higher values (up to -51.6 ppm) are obtained closer to the phenylene rings. Viewing the contributions to the left and right of the phenylene ring shown on the left in Fig. 6 (b), one finds that the local aromaticity on the phenylene ring is clearly reduced as opposed to the neutral form, suggesting that the redox chemistry

(a) – Neutral

(b) – Dication

(c) – Neutral
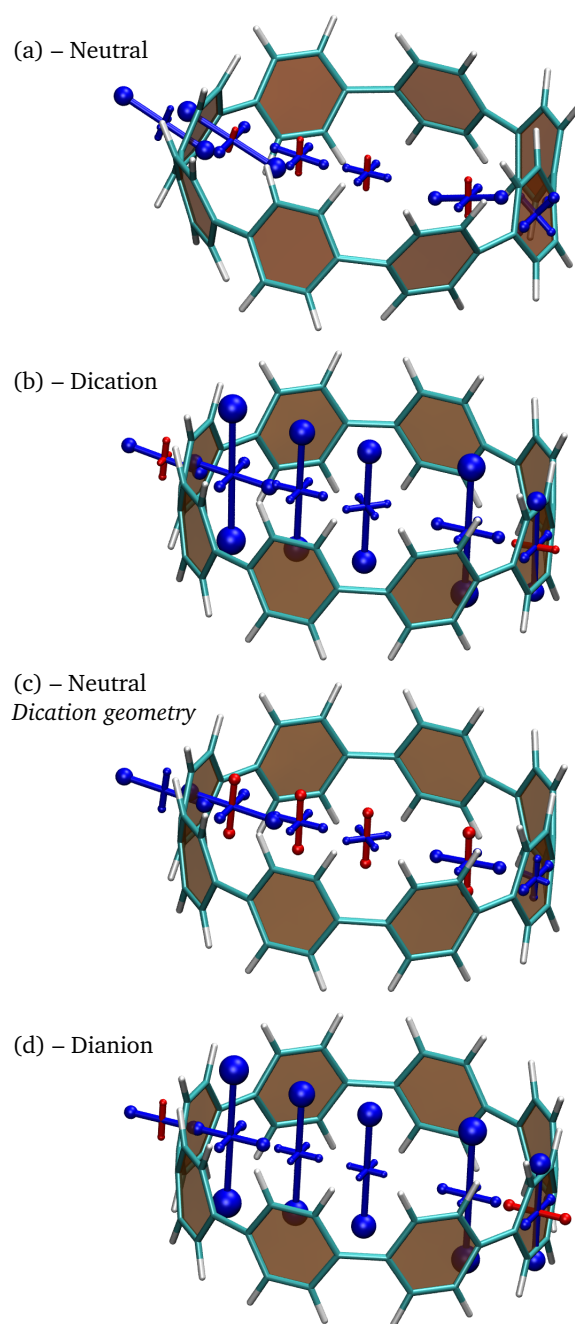*Dication geometry*

(d) – Dianion

Fig. 6 Analysis of local (anti)aromaticity in a [8]CPP. 3D visualisation of the chemical shielding tensors (VIST, see Fig. 2 for details) for (a) the neutral form, (b) the dication, (c) the neutral form at the dication geometry, (d) the dianion.

(a)   B   A   Ni

(b)

(c)

(d)

A: NICS(1) = 9.38(32.2/-1.0/-3.0)
B: NICS(1) = 59.5(184.7/-6.0/-0.4)
Ni: NICS = 47.84(155.3/-5.3/-6.4)

A: NICS(1) = -10.9(-17.6/-10.4/-4.7)
B: NICS(1) = -8.46(-18.9/-5.8/-0.7)
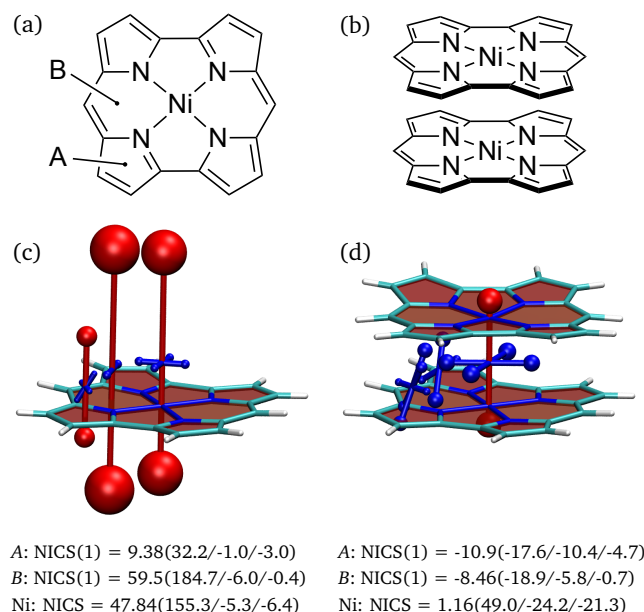Ni: NICS = 1.16(49.0/-24.2/-21.3)

Fig. 7 Analysis of local (anti)aromaticity in a stacked norcorrole dimer: Molecular structures of (a) the monomer and (b) the dimer; 3D visualisation of the chemical shielding tensors (VIST, see Fig. 2 for details) for (c) the monomer and (d) the dimer. NICS values (in ppm) are reported at the positions indicated in (a).

of [8]CPP can be described in terms of a switch between local and global aromaticity similarly to PCT.

Fig. 6 (a) shows that there is no appreciable global antiaromaticity for [8]CPP at its ground state optimised geometry. However, it is interesting to probe whether [8]CPP has a propensity toward antiaromaticity in principle. For this purpose, we have performed computations of the neutral system at the dication geometry. The dication has shorter CC bonds (1.45 *vs* 1.48 Å) and reduced torsion angles (7° *vs* 30°) between adjacent phenylene rings, allowing for enhanced conjugation throughout the macrocycle. The resulting shielding tensors, shown in Fig. 6 (c), highlight that, indeed, the dication geometry leads to enhanced antiaromaticity in the neutral system with NICS components up to 10.3 ppm. We are, thus, left to conclude that the neutral molecule possesses a propensity towards antiaromaticity due to its macrocyclic $4n$ π-electron system but that it has sufficient conformational flexibility to adopt a geometry where antiaromaticity is minimised.

Finally, viewing the dianion in Fig. 6 (d), we find that its chemical shielding structure looks very similar to Fig. 6 (b), highlighting that it exhibits global aromaticity just as the dication.

3.6 Norcorrole dimer – through-space aromaticity

Ni(II) norcorrole [Fig. 7 (a)] is a prominent antiaromatic compound. Its [$4n$] π-electron system cannot escape planarity due to the rigidity of the molecular structure, explaining why strong antiaromaticity is indeed observed in this molecule. Bulky mesityl substituents can be attached to the conjugated core of Ni(II) norcorrole to improve its stability,[85] but the compound is comparatively stable also without these substituents, despite the antiaromaticity.[86] The comparatively high stability of Ni(II) norcorrole makes it an ideal molecule to study stacking interactions between antiaromatic π-conjugated systems and the ensuing emergence of three-dimensional aromaticity. Initially, stacking of flexibly linked Ni(II) norcorrole complexes was investigated,[34] followed by a more recent report of a rigid cyclophane composed of two Ni(II) norcorrole units and two bithiophene linkers.[35] These studies highlighted the importance of through-space currents connecting the two macrocycles.

Within this work, we study the Ni(II) norcorrole complex reported in Ref. 35 but with removed bithiophene linkers, as shown in Fig. 7 (b). Shielding tensors were computed at three different positions, as shown in Fig. 7 (a): 1 Å above the outer 5-membered ring (*A*), 1 Å above the 6-membered ring (*B*), and at the centre of the complex, halfway between the two Ni-atoms (denoted Ni). Starting with the Ni(II) norcorrole monomer [Fig. 7 (c)] we find pronounced antiaromaticity when measured at the Ni and *B* positions with dominant eigenvalues of 185 and 155 ppm, respectively, which are higher than any of the values seen in the above examples. Interestingly, the 5-membered ring (*A*) shows significantly reduced antiaromaticity. This reduction in deshielding for the 5-membered ring, which was also seen in Ref. 23, has been explained in the sense that antiaromatic currents are only present on the inner part of the ring and that norcorrole possesses an aromatic pathway on the perimeter.[22]

To study the effect of stacking between two norcorrole units, we have added a second ring to the system but, otherwise, left the geometry of the first ring and the positions of the chemical shielding tensors unchanged. The striking impact of the second ring is illustrated in Fig. 7 (d): The antiaromaticity disappears for positions *A* and *B* and is strongly reduced at the centre of the complex.

Viewing only the isotropic NICS value at the centre of the ring (1.2 ppm) it is tempting to jump to the conclusion that no relevant shielding effects are present. However, the VIST plot immediately shows that this is incorrect and that the isotropic value is obtained as an average of strong out-of-plane deshielding (49 ppm) in combination with in-plane shielding components of -24 and -21 ppm. Indeed, the shielding observed lies between the $NICS(0)_{zz}$ and $NICS(1)_{zz}$ values for benzene [Fig. 2], thus, indicating the presence of strong aromatic currents. The orientation of these components in parallel to the molecular planes of the norcorrole units is a clear indication that these derive from through-space currents flowing between the two norcorroles.

Closer inspection of the tensors at locations *A* and *B* (see also Fig. S4[†]) shows that these have an unusual shape with their main components tilted with respect to the molecular planes and strong non-orthogonality among the three principal axes of the chemical shielding tensor. We do not attempt to identify the individual ring currents responsible for these results but want to point out that the non-standard electronic structure properties of the norcorrole dimer are reflected by these tensors.

4   Conclusions

Within this article, we presented a method for the visualisation of chemical shielding tensors (VIST) in aromatic and antiaromatic molecules. The VIST method shows the chemical shielding tensor at various points in space around a molecule, thus, allowing to represent the local variations and anisotropy of the chemical shielding in unprecedented clarity. VIST is, thus, particularly useful for large, non-planar molecular systems where it can be exceedingly difficult to obtain the required information otherwise. VIST also provides an expedient route to illustrate the influence of different electronic charge and spin states on (anti)aromaticity.

Within this work, the main properties of the VIST method were

illustrated in the case of planar polycyclic hydrocarbons. Starting with benzene, we investigated how the shape of the shielding tensor changes at different positions surrounding the molecule and highlighted the importance of differentiating between aromatic ring currents and trivial shielding by the electron density. Moving to phenanthrene, we illustrated local variations in aromaticity in this molecule and discussed the shielding tensors in the context of the magnetically induced currents. For cyclobuta[l]phenanthrene the interplay of local aromaticity and antiaromaticity in its singlet state and the emergence of Baird aromaticity in its triplet was studied.

Moving to non-planar macrocycles with competing aromatic and antiaromatic π-systems aligned in different planes illuminated the full power of the VIST method. Starting with PCT, we highlighted the combination of local aromaticity and weak global antiaromaticity in its ground state and a switch to global aromaticity in its doubly reduced state. A similar picture was obtained for [8]CPP, which exhibits pronounced aromatic character in its doubly oxidised and reduced states. The VIST method, thus, provided a clear explanation of the remarkable redox properties of both macrocycles. Finally, studying the stacking between two norcorrole molecules, we showed how strong in-plane antiaromaticity in Ni(II) norcorrole was replaced by weaker in-plane antiaromaticity in combination with through-space aromaticity upon stacking.

Practically, VIST builds on the computation of NICS values and can, thus, be carried out whenever NICS values are available. Moreover, VIST is readily integrated into existing tools used for the visualisation of molecular structures and electron densities. Therefore, we are convinced that VIST constitutes a powerful but also flexible and lightweight computational tool and provides a much-needed extension to the toolbox of chemists studying (anti)aromaticity or using it in their molecular design.

Conflicts of interest

There are no conflicts to declare.

Acknowledgements

Notes and references

1 M. Faraday, *Philos. Trans. R. Soc. London*, 1825, **115**, 440–466.

2 M. B. Smith and J. Michl, *Chem. Rev.*, 2010, **110**, 6891–936.

3 J. Stoycheva, A. Tadjer, M. Garavelli, M. Spassova, A. Nenov and J. Romanova, *J. Phys. Chem. Lett.*, 2020, **11**, 1390–1396.

4 M. Pinheiro, F. B. C. Machado, F. Plasser, A. J. A. Aquino and H. Lischka, *J. Mater. Chem. C*, 2020, **8**, 7793–7804.

5 K. J. Fallon, P. Budden, E. Salvadori, A. M. Ganose, C. N. Savory, L. Eyre, S. Dowland, Q. Ai, S. Goodlett, C. Risko, D. O. Scanlon, C. W. M. Kay, A. Rao, R. H. Friend, A. J. Musser and H. Bronstein, *J. Am. Chem. Soc.*, 2019, **141**, 13867–13876.

6 O. El Bakouri, J. R. Smith and H. Ottosson, *J. Am. Chem. Soc.*, 2020, **142**, 5602–5617.

7 L. Wang, L. Lin, J. Yang, Y. Wu, H. Wang, J. Zhu, J. Yao and H. Fu, *J. Am. Chem. Soc.*, 2020, **142**, 10235–10239.

8 E. Clar, *The aromatic sextet*, Wiley, London, 1972.

9 Z. Sun, Z. Zeng and J. Wu, *Acc. Chem. Res.*, 2014, **47**, 2582–2591.

10 A. Das, T. Müller, F. Plasser and H. Lischka, *J. Phys. Chem. A*, 2016, **120**, 1625–1636.

11 F. Hinkel, J. Freudenberg and U. H. F. Bunz, *Angew. Chem., Int. Ed.*, 2016, **55**, 9830–9832.

12 S. N. Intorp, M. Hodecker, M. Müller, O. Tverskoy, M. Rosenkranz, E. Dmitrieva, A. A. Popov, F. Rominger, J. Freudenberg, A. Dreuw and U. H. Bunz, *Angew. Chem., Int. Ed.*, 2020, **59**, 12396–12401.

13 I. Benkyi, O. Staszewska-Krajewska, D. T. Gryko, M. Jaszuński, A. Stanger and D. Sundholm, *J. Phys. Chem. A*, 2020, **124**, 695–703.

14 T. Dumslaff, Y. Gu, G. M. Paternò, Z. Qiu, A. Maghsoumi, M. Tommasini, X. Feng, F. Scotognella, A. Narita and K. Müllen, *Chem. Sci.*, 2020, **1**, 12816–12821.

15 M. D. Peeks, M. Jirasek, T. D. W. Claridge and H. L. Anderson, *Angew. Chem., Int. Ed.*, 2019, **58**, 15717–15720.

16 M. Rickhaus, M. Jirasek, L. Tejerina, H. Gotfredsen, M. D. Peeks, R. Haver, H.-W. Jiang, T. D. W. Claridge and H. L. Anderson, *Nat. Chem.*, 2020, **12**, 236–241.

17 Y. Han, S. Dong, J. Shao, W. Fan and C. Chi, *Angew. Chem., Int. Ed.*, 2020, anie.202012651.

18 G. V. Baryshnikov, R. R. Valiev, R. T. Nasibullin, D. Sundholm, T. Kurten and H. Ågren, *J. Phys. Chem. A*, 2020, acs.jpca.0c09692.

19 N. Toriumi, A. Muranaka, E. Kayahara, S. Yamago and M. Uchiyama, *J. Am. Chem. Soc.*, 2015, **137**, 82–85.

20 Z. Li, T. Y. Gopalakrishna, Y. Han, Y. Gu, L. Yuan, W. Zeng, D. Casanova and J. Wu, *J. Am. Chem. Soc.*, 2019, **141**, 16266–16270.

21 S. Eder, D. J. Yoo, W. Nogala, M. Pletzer, A. Santana Bonilla, A. J. White, K. E. Jelfs, M. Heeney, J. W. Choi and F. Glöcklhofer, *Angew. Chem., Int. Ed.*, 2020, **59**, 12958–12964.

22 P. B. Karadakov, *Org. Lett.*, 2020, **22**, 8676–8680.

23 S. Y. Liu, H. Kawashima, N. Fukui and H. Shinokubo, *Chem. Commun.*, 2020, **56**, 6846–6849.

24 R. R. Valiev, L. I. Valiulina, H. Fliegl and D. Sundholm, *New J. Chem.*, 2020, **44**, 20643–20650.

25 H. D. Root, D. N. Mangel, J. T. Brewster, H. Zafar, A. Samia, G. Henkelman and J. L. Sessler, *Chem. Commun.*, 2020, **56**, 9994–9997.

26 J.-Y. Shin, T. Yamada, H. Yoshikawa, K. Awaga and H. Shinokubo, *Angew. Chem., Int. Ed.*, 2014, **53**, 3096–3101.

27 J.-Y. Shin, Z. Zhang, K. Awaga and H. Shinokubo, *Molecules*, 2019, **24**, 2433.

28 N. C. Baird, *J. Am. Chem. Soc.*, 1972, **94**, 4941–4948.

29 H. Ottosson, *Nat. Chem.*, 2012, **4**, 969–971.

30 M. D. Peeks, J. Q. Gong, K. McLoughlin, T. Kobatake, R. Haver, L. M. Herz and H. L. Anderson, *J. Phys. Chem. Lett.*, 2019, **10**, 2017–2022.

31 P. B. Karadakov, M. Di and D. L. Cooper, *J. Phys. Chem. A*, 2020, **124**, 9611–9616.

32 D. Yu, C. Rong, T. Lu, P. Geerlings, F. De Proft, M. Alonso and S. Liu, *Phys. Chem. Chem. Phys.*, 2020, **22**, 4715–4730.

33 X. Jiang, S. D. Laffoon, D. Chen, S. Pérez-Estrada, A. S. Danis, J. Rodríguez-López, M. A. Garcia-Garibay, J. Zhu and J. S. Moore, *J. Am. Chem. Soc.*, 2020, **142**, 6493–6498.

34 R. Nozawa, H. Tanaka, W.-Y. Cha, Y. Hong, I. Hisaki, S. Shimizu, J.-Y. Shin, T. Kowalczyk, S. Irle, D. Kim and H. Shinokubo, *Nat. Commun.*, 2016, **7**, 13620.

35 R. Nozawa, J. Kim, J. Oh, A. Lamping, Y. Wang, S. Shimizu, I. Hisaki, T. Kowalczyk, H. Fliegl, D. Kim and H. Shinokubo, *Nat. Commun.*, 2019, **10**, 3576.

36 Y. Ni, T. Y. Gopalakrishna, H. Phan, T. Kim, T. S. Herng, Y. Han, T. Tao, J. Ding, D. Kim and J. Wu, *Nat. Chem.*, 2020, **12**, 242–248.

37 J. Michl, *Pure Appl. Chem.*, 2008, **80**, 429–446.

38 R. V. Williams, *Chem. Rev.*, 2001, **101**, 1185–1204.

39 P. B. Karadakov and D. L. Cooper, *J. Phys. Chem. A*, 2016, **120**, 8769–8779.

40 T. Stauch, *Chem. - Eur. J.*, 2018, **24**, 7340–7344.

41 N. Li, B. Wu, C. Yu, T. Li, W. X. Zhang and Z. Xi, *Angew. Chem., Int. Ed.*, 2020, **59**, 8868–8872.

42 E. Hückel, *Zeitschrift für Phys.*, 1931, **70**, 204–286.

43 W. Kutzelnigg, *J. Comput. Chem.*, 2007, **28**, 25–34.

44 D. Geuenich, K. Hess, F. Köhler and R. Herges, *Chem. Rev.*, 2005, **105**, 3758–3772.

45 H. Fliegl, S. Taubert, O. Lehtonen and D. Sundholm, *Phys. Chem. Chem. Phys.*, 2011, **13**, 20500–20518.

46 Z. Chen, C. S. Wannere, C. Corminboeuf, R. Puchta and P. von Ragué Schleyer, *Chem. Rev.*, 2005, **105**, 3842–3888.

47 C. Corminboeuf, T. Heine, G. Seifert, P. Von Ragué Schleyer and J. Weber, *Phys. Chem. Chem. Phys.*, 2004, **6**, 273–276.

48 J. C. Facelli, *Magn. Reson. Chem.*, 2006, **44**, 401–408.

49 P. Von Ragué Schleyer, M. Manoharan, Z. X. Wang, B. Kiran, H. Jiao, R. Puchta and N. J. Van Eikema Hommes, *Org. Lett.*, 2001, **3**, 2465–2468.

50 S. Klod and E. Kleinpeter, *J. Chem. Soc. Perkin Trans. 2*, 2001, 1893–1898.

51 T. Heine, C. Corminboeuf and G. Seifert, *Chem. Rev.*, 2005, **105**, 3889–3910.

52 R. Gershoni-Poranne and A. Stanger, *Chem. - Eur. J.*, 2014, **20**, 5673–5688.

53 A. Stanger, G. Monaco and R. Zanasi, *ChemPhysChem*, 2020, **21**, 65–82.

54 B. J. Lampkin, P. B. Karadakov and B. VanVeller, *Angew. Chem., Int. Ed.*, 2020, **59**, 19275–19281.

55 V. Vijay, M. Madhu, R. Ramakrishnan, A. Benny and M. Hariharan, *Chem. Commun.*, 2019, **56**, 225–228.

56 J. R. Cheeseman, *J. Chem. Phys.*, 1996, **104**, 5497–5509.

57 J. C. Facelli, *Prog. Nucl. Magn. Reson. Spectrosc.*, 2011, **58**,

176–201.

58 T. Helgaker, S. Coriani, P. Jørgensen, K. Kristensen, J. Olsen and K. Ruud, *Chem. Rev.*, 2012, **112**, 543–631.

59 P. W. Atkins, *Physical Chemistry*, Oxford University Press, Oxford, 5th edn, 1994.

60 N. F. Ramsey, *Phys. Rev.*, 1950, **78**, 699–703.

61 E. Steiner and P. W. Fowler, *Chem. Commun.*, 2001, **1**, 2220–2221.

62 D. Sundholm, H. Fliegl and R. J. Berger, *Wiley Interdiscip. Rev. Comput. Mol. Sci.*, 2016, **6**, 639–678.

63 M. J. Frisch, G. W. Trucks, H. B. Schlegel, G. E. Scuseria, M. A. Robb, J. R. Cheeseman, G. Scalmani, V. Barone, B. Mennucci, G. A. Petersson, H. Nakatsuji, M. Caricato, X. Li, H. P. Hratchian, A. F. Izmaylov, J. Bloino, G. Zheng, J. L. Sonnenberg, M. Hada, M. Ehara, K. Toyota, R. Fukuda, J. Hasegawa, M. Ishida, T. Nakajima, Y. Honda, O. Kitao, H. Nakai, T. Vreven, J. A. Montgomery, Jr., J. E. Peralta, F. Ogliaro, M. Bearpark, J. J. Heyd, E. Brothers, K. N. Kudin, V. N. Staroverov, T. Keith, R. Kobayashi, J. Normand, K. Raghavachari, A. Rendell, J. C. Burant, S. S. Iyengar, J. Tomasi, M. Cossi, N. Rega, J. M. Millam, M. Klene, J. E. Knox, J. B. Cross, V. Bakken, C. Adamo, J. Jaramillo, R. Gomperts, R. E. Stratmann, O. Yazyev, A. J. Austin, R. Cammi, C. Pomelli, J. W. Ochterski, R. L. Martin, K. Morokuma, V. G. Zakrzewski, G. A. Voth, P. Salvador, J. J. Dannenberg, S. Dapprich, A. D. Daniels, O. Farkas, J. B. Foresman, J. V. Ortiz, J. Cioslowski and D. J. Fox, *Gaussian09 Revision E.01*, 2013, Gaussian Inc. Wallingford CT.

64 J. P. Perdew, K. Burke and M. Ernzerhof, *Phys. Rev. Lett.*, 1996, **77**, 3865–3868.

65 C. Adamo and V. Barone, *J. Chem. Phys.*, 1999, **110**, 6158–6170.

66 A. Schafer, H. Horn and R. Ahlrichs, *J. Chem. Phys.*, 1992, **97**, 2571–2577.

67 F. Plasser and H. Lischka, *J. Chem. Theory Comput.*, 2012, **8**, 2777–2789.

68 F. Plasser, M. Wormit and A. Dreuw, *J. Chem. Phys.*, 2014, **141**, 024106.

69 F. Plasser, *J. Chem. Phys.*, 2020, **152**, 084108.

70 W. Humphrey, A. Dalke and K. Schulten, *J. Mol. Graphics*, 1996, **14**, 33 – 38.

71 H. Fliegl, D. Sundholm, S. Taubert, J. Jusélius and W. Klopper, *J. Phys. Chem. A*, 2009, **113**, 8668–8676.

72 Supporting research data available: Molecular geometries, Gaussian input/output files, input scripts for VMD. DOI: 10.17028/rd.lboro.13546826 .

73 A. Stanger, *J. Org. Chem.*, 2006, **71**, 883–893.

74 M. Solà, *Front. Chem.*, 2013, **1**, 4–11.

75 P. B. Karadakov, *J. Phys. Chem. A*, 2008, **112**, 7303–7309.

76 R. Ayub, O. E. Bakouri, K. Jorner, M. Solà and H. Ottosson, *J. Org. Chem.*, 2017, **82**, 6327–6340.

77 S. Horn, F. Plasser, T. Müller, F. Libisch, J. Burgdörfer and H. Lischka, *Theor. Chem. Acc.*, 2014, **133**, 1511.

78 H. Lischka, D. Nachtigallová, A. J. A. Aquino, P. Szalay, F. Plasser, F. B. C. Machado and M. Barbatti, *Chem. Rev.*, 2018, **118**, 7293–7361.

79 S. Pathak, R. Bast and K. Ruud, *J. Chem. Theory Comput.*, 2013, **9**, 2189–2198.

80 S. E. Lewis, *Chem. Soc. Rev.*, 2015, **44**, 2221–2304.

81 B. M. Wong, *J. Phys. Chem. C.*, 2009, **113**, 21921–21927.

82 L. Stojanović, S. G. Aziz, R. H. Hilal, F. Plasser, T. A. Niehaus and M. Barbatti, *J. Chem. Theory Comput.*, 2017, **13**, 5846–5860.

83 T. Iwamoto, Y. Watanabe, T. Sadahiro, T. Haino and S. Yamago, *Angew. Chem., Int. Ed.*, 2011, **50**, 8342–8344.

84 E. J. Leonhardt and R. Jasti, *Nat. Rev. Chem.*, 2019, **3**, 672–686.

85 T. Ito, Y. Hayashi, S. Shimizu, J.-Y. Shin, N. Kobayashi and H. Shinokubo, *Angew. Chem., Int. Ed.*, 2012, **51**, 8542–8545.

86 S. Ukai, Y. H. Koo, N. Fukui, S. Seki and H. Shinokubo, *Dalt. Trans.*, 2020, **49**, 14383–14387.

<div align="center">

Electronic Supporting Information

for

3D Visualisation of chemical shielding tensors (VIST) to elucidate aromaticity and antiaromaticity

F. Plasser, F. Glöcklkhofer

January 14, 2021

</div>

Contents

Section S1 - Left eigenvectors and complex eigenvalues

The shielding tensor is in general represented by a non-symmetric matrix, which gives rise to two technical issues, which we shall discuss briefly in the following: (i) the presence of left eigenvectors and (ii) the occurrence of complex eigenvalues. In Eq. (6) of the main manuscript we have considered the right eigenvectors of the chemical shielding tensor and we will use these in the following unless noted otherwise. Alternatively, it would be possible to do the same decomposition using the left eigenvectors

$$\sum_{\gamma \in \{x,y,z\}} l_\gamma^{(i)} \sigma_{\gamma\beta} = l_\beta^{(i)} t^{(i)} \qquad\qquad i \in \{1,2,3\} \qquad\qquad (S1)$$

This would yield the same eigenvalues $t^{(i)}$ as Eq. (6), considering that they are determined as the roots of the same characteristic polynomial, but it would generally produce different principal axes. Note that the two equations differ in the sense that the summation in Eq. (6) goes over the components of magnetic field B_β whereas the summation in Eq. (S1) is performed with respect to the formal nuclear moments μ_γ. It is not *a priori* clear which representation is better. In practice, we have found that the representations have a similar appearance only that the left eigenvectors are a bit tilted with respect to the right ones. To exemplify this, we show the right and left eigenvectors in Fig. S2 (b,c) and (d,e), respectively. First, it is noted that the left eigenvalues are the same as the right eigenvalues meaning that the length of the axes and size of the spheres is the same. In the case of the NICS(0) tensors, we also find that, due to symmetry reasons the left eigenvectors are exactly the same as the right ones. When viewing the NICS(1) tensors we find that the left eigenvectors are somewhat tilted with respect to the molecular plane but that they, otherwise, have a similar appearance to the right eigenvectors. We found the same conclusion also for other examples: the left eigenvectors are similar to the right eigenvectors with the exception of being slightly tilted. We, thus, continue by viewing only the right eigenvectors and suggest using these for future applications.
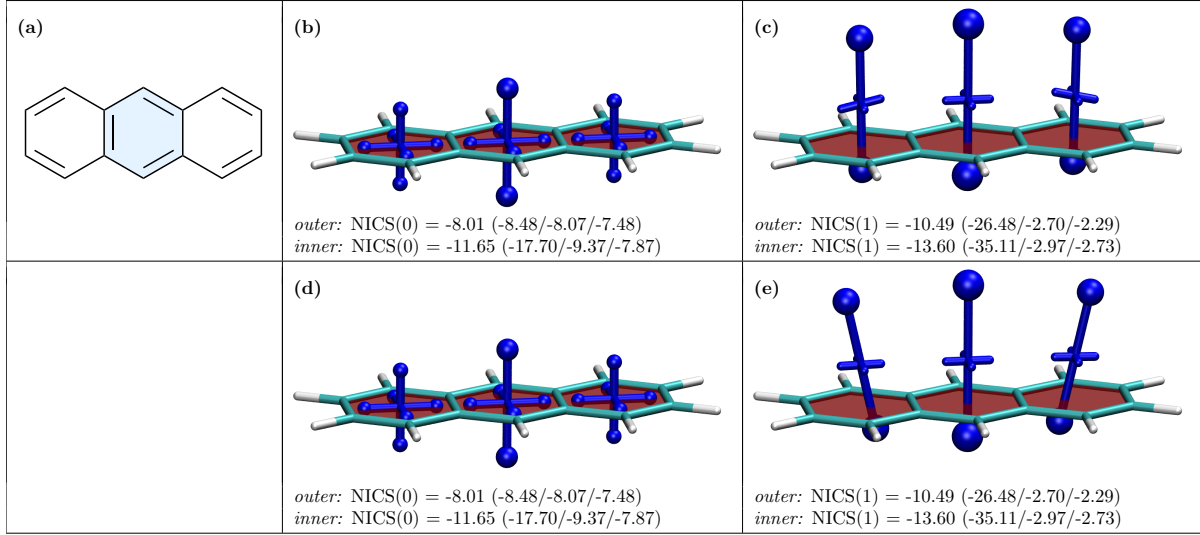
Figure S1: Analysis of local aromaticity in anthracene: **(a)** molecular structure with Clar sextet highlighted in blue; 3D representation of the chemical shielding tensors using the right eigenvectors computed at **(b)** the centre of each ring and **(c)** 1Å above the plane; **(d)** and **(e)** same as above using the left eigenvectors. NICS values (in ppm) are reported for the *outer* and *inner* rings.

Finally, we want to discuss the case where one of the eigenvalues, e.g. $t^{(1)}$, is a complex number. In this case, we use a mathematical formalism similar to the construction of two-dimensional real representations of cyclic symmetry groups. Due to the fact that the σ-matrix is real, it follows that if $t^{(1)}$ is complex, also its complex conjugate $t^{(1)*}$ is an eigenvalue and that the associated eigenvector is the complex conjugate of $\vec{q}^{(1)}$. In summary, we can write

$$t^{(2)} = t^{(1)*} \qquad\qquad \vec{q}^{(2)} = \vec{q}^{(1)*} \qquad\qquad (S2)$$

Noting this relation, we use the following three vectors as a basis for the coordinate system: $\text{Re}(\vec{q}^{(1)}), \text{Im}(\vec{q}^{(1)}), \vec{q}^{(3)}$ where Re and Im denote the real and imaginary parts of the vectors. The associated diagonal matrix elements are $\text{Re}(t^{(1)}), \text{Re}(t^{(1)}), t^{(3)}$ noting that these conserve the trace in analogy to Eq. (8) of the main text, i.e.

$$\sigma_{\text{iso}} = \frac{1}{3}\left(\text{Re}(t^{(1)}) + \text{Re}(t^{(1)}) + t^{(3)}\right) \qquad\qquad (S3)$$

Section S2 - Benzene

(a)   (b)   (c)

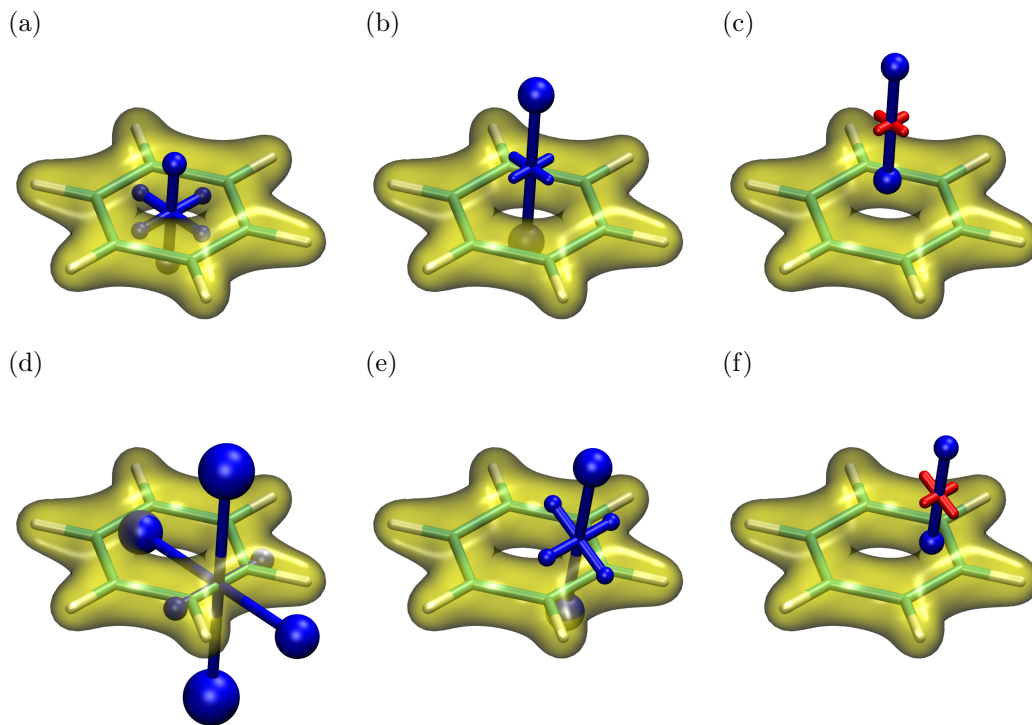(d)   (e)   (f)

Figure S2: 3D visualisation of the chemical shielding tensors (VIST) in benzene. Negative (shielded/aromatic) contributions are shown in blue, positive (deshielded, antiaromatic) in red. Shielding tensors were computed at (a) the centre of the molecule, (b) 1 Å and (c) 2 Å above the plane; (d) at the centre of a bond, (e) 1 Å and (f) 2 Å above the bond. The electron density is shown in yellow (isovalue 0.1 a.u., encompassing about 60% of the total electron density).

Section S3 - Paracyclophanetetraene
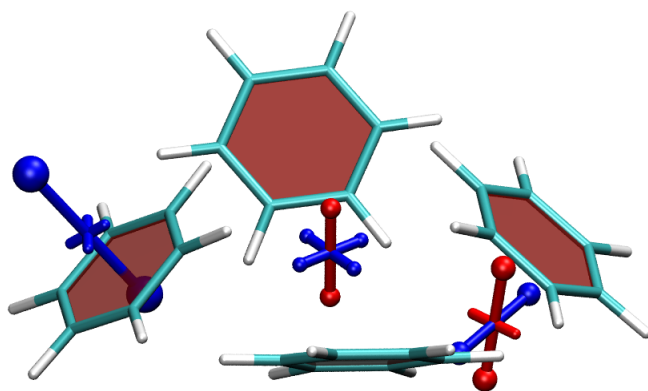
A: NICS(1) = -11.23 (-29.70/-2.26/-1.74)
B: NICS(0) = -0.31 (9.39/-5.16/-5.16)
C: NICS(0) = 1.31 (13.61/-12.18/2.49)

Figure S3: 3D visualisation of the chemical shielding tensors (VIST) of four isolated benzene rings arranged according to the geometry of PCT in its singlet ground state. This figure shows that deshielding at positions B and C is also present for isolated benzene rings but that it is notably enhanced in the macrocycle.

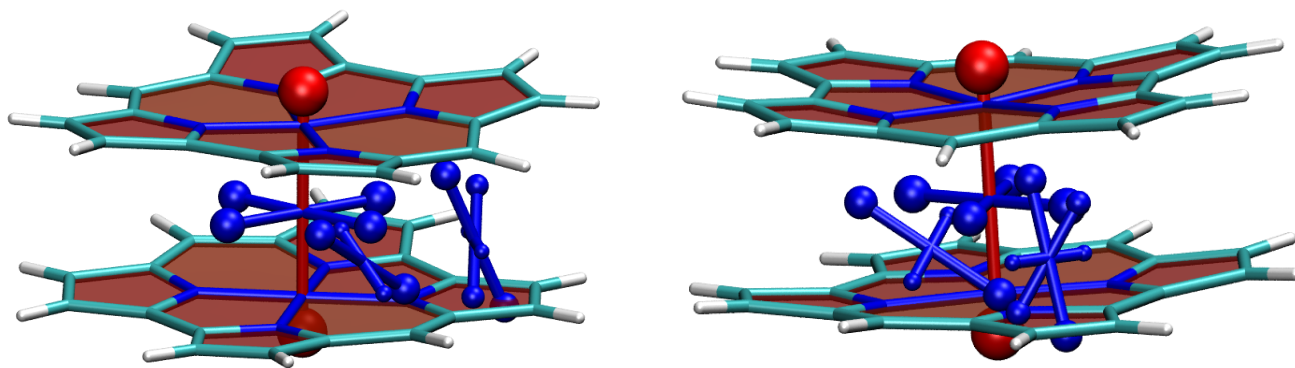# Section S4 - Norcorrole dimer

Figure S4: 3D visualisation of the chemical shielding tensors (VIST) in the norcorrole dimer using alternative viewing angles.